Localized Surface Plasmon Resonance Biosensor: An Improved Technique for SERS Response Intensification

MD. SAIFUL ISLAM[1,2,*], JAKEYA SULTANA[1], RIFAT AHMMED AONI[3], MD. SELIM HABIB[4], ALEX DINOVITSER[1], BRIAN W.-H. NG[1], AND DEREK ABBOTT[1]

[1] The University of Adelaide, School of Electrical & Electronic Engineering, Adelaide, 5005, Australia
[2] Institute of Photonics & Advance Sensing (IPAS), University of Adelaide, SA 5005, Australia.
[3] Nonlinear Physics Centre, Research School of Physics and Engineering, Australian National University, Canberra, Acton 2601, Australia.
[4] The College of Optics and Photonics, University of Central Florida, USA.
[*] Corresponding author: mdsaiful.islam@adelaide.edu.au

Compiled January 15, 2019

As technology continues to advance, the development of novel sensing systems opens up new possibilities for low cost, practical biosensing applications. In this paper, we demonstrate a localized surface plasmon resonance (LSPR) system that combines both wave-guiding and plasmonic resonance sensing with a single microstructured polymeric structure. Characterizing the sensor using Finite Element Method (FEM) simulation results show a record wavelength sensitivity (WS) of 111000 **nm/RIU, high amplitude sensitivity (AS) of** 2050 **RIU^{-1}, high sensor resolution and limit of detection (LOD) of** 9×10^{-7} **RIU and** 8.12×10^{-12} **RIU^2/nm respectively. Furthermore, these sensors have the capability to detect an analyte within the refractive index (RI) range of** 1.33 **to** 1.43 **in the visible to mid-IR therefore being potentially suitable for applications in biomolecular and chemical analyte detection.**

http://dx.doi.org/10.1364/ao.XX.XXXXXX

LSPR is an optical phenomenon that is a result of surface plasmon excitation in nanoparticles or nanogratings of size smaller than the wavelength of light. The high optical confinement and local field enhancement capability of LSPR are widely implemented for surface-enhanced Raman scattering (SERS) analysis where enhanced electromagnetic fields near metal nanostructure promote significant Raman response of deposited proteins/molecules that are in contact with the metal [1, 2]. The use of photonic crystal fiber (PCF) has advantages in terms of tunability, size, and immunity to electromagnetic interference in combination with LSPR makes the sensor suitable for a range of sensing applications. For bioanalyte detection and SERS response intensification several studies with different techniques including surface plasmon resonance (SPR) and LSPR have been carried out [4–6, 9]. Using tungsten disulfide to support SPR, sensitivity of 2459.3 nm/RIU for RI ranging from 1.33 to 1.36 has been reported [4]. Using a D-shaped fiber structure researchers obtained a maximum WS of 44567 nm/RIU [5]. Note that, recent studies [4–6, 9] were carried out using SPR technology and used either internal sensing or external sensing using a D-shaped structure. In internal sensing, the filling and flushing of the analyte is challenging, whereas the D-shaped PCF requires external surface polishing to give its shape. Here, internal sensing refers to filling various air holes of the fiber with the analyte solution—this can be carried out via a syringe (ie. withdrawal or pumping mode)—whereas external sensing refers to contacting the analyte to the fiber surface. Note that, our recent study on SPR showed a high WS (62000 nm/RIU) and AS (1415 RIU^{-1}) that comes with high confinement loss (CL) (300 dB/cm) [8]. However, it has been necessary to eliminate thick cladding layers from these fibers to allow fields to interact directly through evanescent waves arising from the core/cladding boundary region, resulting in a loss of mechanical strength. Therefore, LSPR based sensors are introduced as a solution to enhance the sensing performance as well as minimizing the size and cost [7, 9]. Using nanospheres, researchers were able to achieve a maximum WS of 27000 nm/RIU [7] whereas the use of a Au grating reports a maximum WS of 3340 nm/RIU with extremely low AS that also comes with high CL [9]. Therefore, there is scope to develop an improved theoretical framework of PCF based biosensors that may eventually lead to different practical implementations in both the medical and chemical industries.

In this letter, we aim to design a sensor that can improve the absorption, resolution, and LOD with low CL. Therefore we propose a dual channel based LSPR sensor having a Au grating as a plasmonic metal with the analyte channel in contact with Au that facilitates external sensing. Considering the fabrication feasibility, we describe the optimized sensor by analysing different structures with variations in key geometrical parameters.

The design (Fig. 1 (a)) and computational analysis of the sensor are carried out using COMSOL multiphysics 5.3 set to an extremely fine mesh size with a degree of freedom of 739945, number of elements of 105616, and minimum element quality of 0.324. On a silica (SiO_2) substrate the air holes are placed in such a way that so as to confine the electric field to the center of the fiber and interact strongly with the metal. A thinner TiO_2 layer is used in contact with the SiO_2 so that the Au can adhere strongly to SiO_2. The basic data for the model, such as the RI

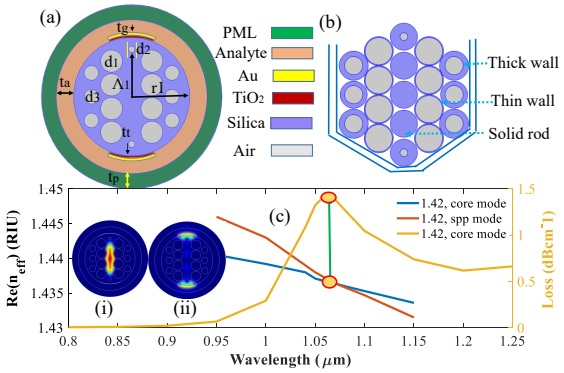

Fig. 1. (a) Schematic of the cross section; (b) stacked preform and (c) dispersion relation between core guided mode, plasmonic mode and loss spectra at the core mode having the inset of (c) shows the electromagnetic field distribution (i) core mode and (ii) SPP mode.

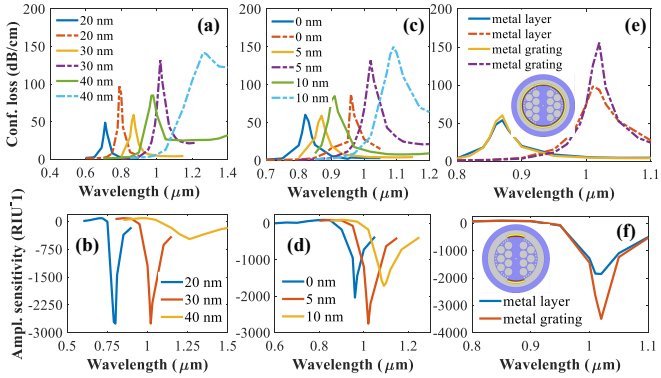

Fig. 2. (a–b) CL and AS with t_g variation; (c–d) CL and AS with t_t variation; and (e–f) CL and AS having SPR and LSPR.

of SiO_2, TiO_2, and Au is obtained from ref. [14–16]. The air hole diameters are defined as d_1, d_2, and d_3, the outer surface radius and pitch from the center to d_2 are defined as r_1 and Λ_1, and TiO_2, Au, analyte and the perfectly matched layer (PML) thicknesses are defined as t_t, t_g, t_a, and t_p respectively. Note that the PML is an computational boundary that absorbs scattered waves from the PCF. The scaled down air holes of diameter d_2 and d_3 help to reduce the CL as it contributes to reduced scattering of light from the center of the fiber. The stacked capillary diagram of the sensor is shown in Fig. 1 (b) showing that it can be fabricated using capillary stacking. In terms of fabrication the thicker wall capillary indicates smaller air holes and solid rods indicate no air holes. Fig. 1 (c) indicates that when the phase matching of $\mathrm{Re}(n_{\mathrm{eff}})$ between the core guided mode and SPP mode occurs then the sensor is then at resonance and thus a maximum loss peak is obtained. Inset of Fig. 1 (c) shows the electric field distribution in the core guided mode (i) and SPP mode (ii).

We considered $d_c = 0.18\Lambda$, $d = 0.70\Lambda$, $d_1 = 0.09\Lambda$, $\Lambda = 3.75$ μm, $t_a = 1.5$ μm, $t_p = 1.80$ μm and varied the Au and TiO_2 thickness respectively to get optimum t_g and t_t, and then at optimum t_g and t_t we characterise the sensor with SPR and LSPR.

Starting with Au we vary the t_g to 20 nm, 30 nm and 40 nm and the obtained characteristics that are shown in Fig. 2 (a)–(b). Comparing 20 nm and 30 nm we can see that the obtained CL for 20 nm is less than 30 nm. Though the AS is almost the same (2754 RIU^{-1} for 20 nm and 2752 RIU^{-1} for 30 nm), the WS for 30 nm is higher (15000 nm/RIU) than 20 nm (8000 nm/RIU). Therefore we choose 30 nm as optimum. Now, comparing 30 nm with 40 nm we see that the loss peak broaden at 40 nm thus the AS also reduces in a large scale as shown in Fig. 2 (a)–(b). Thus considering the loss, WS and AS we consider 30 nm as the optimum Au thickness. Here the CL, WS, and AS are calculated using the equation $8.686\frac{2\pi}{\lambda}\mathrm{Im}(n_{\mathrm{eff}}) \times 10^4(\mathrm{dB/cm})$; $\frac{\Delta\lambda_{\mathrm{peak}}}{\Delta n_a}(\mathrm{nm/RIU})$ and $-\frac{1}{\alpha(\lambda,n_a)}\frac{\delta\alpha(\lambda,n_a)}{\delta n_a}$ (RIU^{-1}) [8] respectively, where λ indicates the operating wavelength in microns, $\mathrm{Im}(n_{\mathrm{eff}})$ is the imaginary part of the complex RI of the core mode, $\Delta\lambda_{\mathrm{peak}}$ denotes the wavelength difference between the loss peak shift and Δn_a indicates the change in analyte RI, $\alpha(\lambda, n_a)$ is the overall loss and the difference between two loss spectra due to a small change of analyte RI is denoted by $\delta\alpha(\lambda, n_a)$.

The optimization of TiO_2 is illustrated in Fig. 2 (c)–(d). It indicates that without TiO_2 the CL is low, however that comes with low WS and AS because TiO_2 has a high RI and acts as a transition metal and when placed between SiO_2 and Au it generates large number of electrons at the surface. This creates a strong evanescent wave and attracts the fields from the core guided mode to interact strongly with the plasmonic mode and therefore increases CL, which also increases the sensitivity. Without the TiO_2 coating, the plasmonic Au exhibits poor adhesion to the SiO_2, and easily flakes off with light pressure [10]. To provide proper adhesion, a thin layer of TiO_2 is included to provide the necessary adhesion. A 10 nm coating between the SiO_2 and the Au, increases the CL and broadens the loss peak. However, a slightly thinner layer (5 nm), is found to restore the sharp loss peak, required to achieve the high AS.

The reason for utilizing LSPR instead of SPR is shown in Fig. 2 (e-f). We observe that with LSPR a sharper loss peak results in around 1.85 times larger AS than with SPR. In LSPR, excitation of surface electrons occurs over a small portion of surface that results in lowering the CL. This is because plasmons are only created in a localized area and not on the whole surface. Note that, this is also the reason for obtaining sharper loss peak as fields from the core can strongly interact with the specified portion of the surface. The corresponding WS and AS with LSPR and SPR are 14000 nm/RIU, 15000 nm/RIU and 3500 RIU^{-1}, 1900 RIU^{-1} respectively. Moreover, LSPR requires less Au and TiO_2, which may result in improved cost effectiveness for real-world applications. Note that, in Fig. 2, Fig. 3 and Fig. 4 the solid and dashed lines indicates the performance for RI of 1.41 and 1.42 respectively.

Considering the LSPR at optimum Au and TiO_2 thickness we then optimize the analyte and PML. We start with the analyte layer and vary it to 1.2 μm, 1.5 μm, 1.8 μm and 2.1 μm. The characteristics shown in Fig. 3 (a)–(b) illustrate that at low t_a, the sensor experiences low loss, however that comes with low AS (1350 RIU^{-1}). As t_a increases, the loss peaks begin sharpening and a sharper loss peak is obtained at $t_a = 1.8$ μm. Therefore, maximum AS (3500 RIU^{-1}) is obtained at that thickness. Increasing from 1.8 μm we can see that the AS starts to decrease. Therefore, considering the loss peak broadening and AS, we choose 1.8 μm as the optimum t_a. Then, keeping t_a fixed to 1.8 μm with other optimal design parameters we optimize the t_p. We can see that at $t_p = 1.50$ μm the AS is low as compared to $t_p = 1.80$ μm and 2.1 μm. However when we increase t_p to 1.80 μm the AS also increases and any further increase of PML

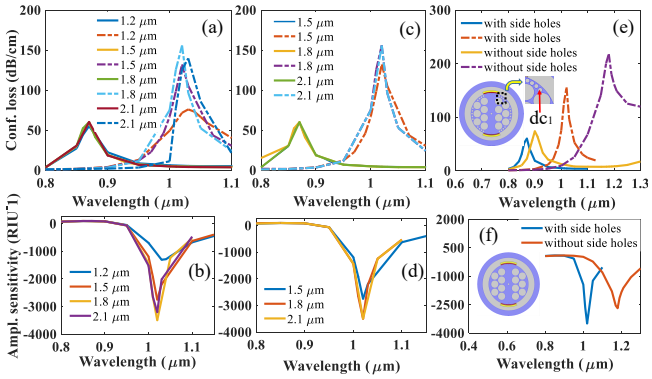

Fig. 3. (a–b) CL and AS having t_a variation; (c–d) CL and AS having t_p variation; and (e–f) CL and AS having side air holes near the surface.

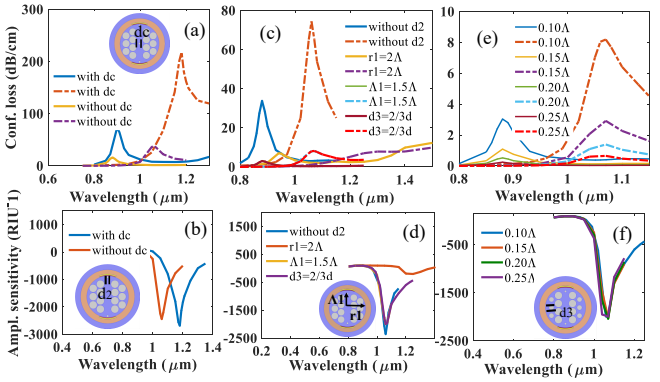

Fig. 4. (a–b) CL and AS of the LSPR sensor with and without d_c; (c–d) CL and AS having the effect of d_2, the outer surface radius (r_1), the pitch Λ_1 and the air holes of diameter d_3; and (e–f) CL and AS having different size of d_2.

does not change the characteristics of the fiber sensor. Therefore we choose 1.80 μm as the optimum PML thickness.

Till now we have optimized different geometrical parameters including selection between SPR and LSPR by considering few smaller shaped air holes of diameter $d_{c_1} = d_c$ closest to the sensing surface as shown in Fig. 2 (e)–(f) and Fig. 3 (e). The reason for utilizing such small air holes is to help confine more light into the core and prevent light from being scattered out to the surface. We can see from Fig. 3 (e-f) that with d_{c_1} near the surface the sensor shows a remarkable AS with sharper loss peak. However, a number of holes close to the surface creates fabrication difficulties. The reason is, there is insufficient space near the surface to place the same sized capillary to produce the smaller air holes. One possible solution may be to use a smaller size capillary outer diameter. However, different sized holes during the fibre drawing process is problematic in terms of maintaining even pressure through all the holes. Considering this fact and in order to simplify the design, we remove d_{c_1} and characterize the sensor. We find that (Fig. 3 (e-f)) removing d_{c_1} reduces the sensing performance and increases the loss (AS reduces to 2850 RIU^{-1} from 3500 RIU^{-1}). However, considering feasibility of fabrication we choose the sensor without d_{c_1} as optimum (as shown inset of Fig. 3 (f)).

The analysis illustrated in Fig. 2 & Fig. 3 shows that the optimized sensor exhibits very high CL, which is a limitation in terms of practical implementations of the sensor because it also limits the sensor length. Note that, we place an air hole at the center of diameter $d_c = d_2 = 0.18\Lambda$ so that it can deflect the electromagnetic waves from the center towards the metal dielectric interface. The motivation is to enhance the light-matter interaction, however that comes with a high CL. We find that removal of d_c decreases the CL from 73 dB/cm to 16 dB/cm for an analyte RI 1.41 and from 218 dB/cm to 39 dB/cm for an analyte RI of 1.42. We find that the resulting change in WS and AS is almost negligible, as shown in Fig. 4 (a-b). Therefore considering the CL we choose the sensor structure without d_c as optimum.

The fabrication of the fiber shown in Fig. 4 (b) is challenging because of the position of d_2 so close to the surface. It is impossible to place a capillary of size d_1 at the position of d_2 and maintain the shape of the surface. Several solutions to these problems have been considered, including (i) removing d_2, (ii) increasing the radius of outer surface r_1 and (iii) reducing the pitch distance Λ_1 of d_2 from center, or (iv) machining the surface of the silica preform after fabrication. We characterize the sensor considering all the possible solutions and the obtained characteristics are shown in Fig. 4 (c–d). We started by removing d_2 and found that a high AS of 2360 RIU^{-1} can be obtained, but with a high CL of 34 dB/cm for 1.41 and 75 dB/cm for 1.42 than with d_2. This is because without d_2 the electromagnetic waves from the center of the fiber interact directly with the plasmonic metal that assists in creating high sensitivity, however this comes at the price of large scattering that results in high CL. Therefore, it is important to limit the scattering of light and thus we decide to retain d_2, but with optimized position so that loss can be reduced further maintaining sensitivity and fabrication feasibility.

Next, keeping d_2 in its previous position ($\Lambda_1 = 1.75\Lambda$) we then increased the radius of the outer surface (r_1) from where we find an extremely low AS of 122 RIU^{-1} with broadening of loss peak. Therefore without varying r_1, we place d_2 in a position where capillaries of diameter d_1 can be used to create both hole sizes required for this design. As such we reduce the pitch ($\Lambda_1 = 1.5\Lambda$) of d_2 and maintain sufficient space from the surface to the air hole. Fabrication will use pressurization of the capillaries to achieve the desired size of d_2. We can see the resulting characteristics (from Fig. 4 (c–d)) with extremely low CL (3 dB/cm for 1.41 and 8 dB/cm for 1.42). The optimized sensor (shown in Fig. 4 (d)) also exhibits a high AS of 2050 RIU^{-1}and WS of 111000 nm/RIU.

However, in the present optimized structure there is another problem that is still challenging for fabrication. We can see that (as shown in the inset of Fig. 4 (d)) the air hole of diameter d_3 is still close to the surface that may also be a challenge for fabrication. Note that it is necessary to keep d_3 so that it can act as an obstacle for scattered light from the core and assist with tighter confinement at the center of the fiber. Considering the fabrication difficulties there are two possible solutions to facilitate fabrication. One is to increase (r_1) and the another is to reduce the diameter of d_3 and characterise the sensing performance. Previously we observed that increasing r_1 dramatically reduces the AS and therefore the only option now is to reduce d_3. Reducing d_3 to $d_3 = 2/3d$ we can see that the CL, AS and WS has not change notably. The reason is the pitch distance between the air holes (d_1) in first ring of cladding. Note that, the reduced diameter for d_3 is still larger than the spacing between air holes of diameter d_1. Therefore, d_3 are able to reflect back the scattered light inside the center of the fiber to maintain the performance with easier fabrication. Therefore, we choose $d_3 = 2/3d_1$ as

optimum diameter in the second ring of the cladding.

Note that, the size of d_2 have also impact on CL and sensitivity therefore we also optimize it that is shown in Fig. 4 (e-f). We found that, increasing size of d_2 decreases the CL however careful attention should also be given to choose optimum d_2 so that light wave get sufficient path to interact with the plasmonic metal at the surface. A larger diameter of d_2 act as an obstacle of interacting the light from the core with the portion of metal surface. Therefore, after a certain diameter of d_2, with reduction of CL the WS and AS also start to reduce and loss peak starts to get broad again. Thus, considering both CL, WS and AS we choose $d_2 = 0.20\Lambda$ as optimum.

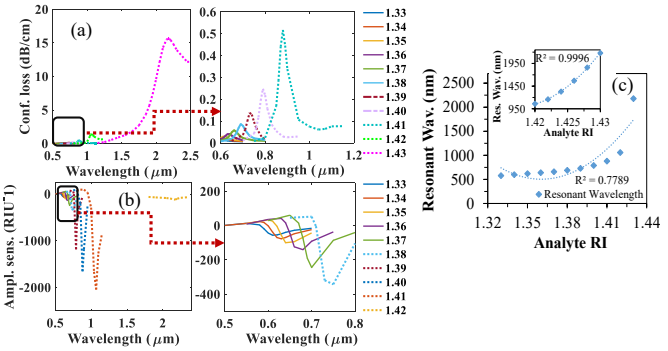

Fig. 5. (a) CL, (b) AS and (c) fibre linearity having optimized geometrical parameters of the sensor.

The CL and sensitivity experienced by the sensor with changing of RI is shown in Fig. 5 (a-b). It can be seen from Fig. 5 (a-b) that the sensor is highly sensitive with the change of environment RI that also comes with negligible CL. The losses at resonance peaks for analyte RI 1.33 to 1.43 are found to be 0.02, 0.024, 0.03, 0.041, 0.058, 0.087, 0.14, 0.25, 0.52, 1.43, and 15.63 dB/cm (Fig. 5 (a)) which are extremely low with corresponding resonance peak wavelengths of 580, 600, 620, 640, 660, 690, 730, 790, 880, 1060, and 2180 nm. Note that, the increment of CL with RI is due to lower penetration of electromagnetic field towards the core and higher penetration towards the LSPR region. Therefore according to the resonance peak shift we obtain a record WS of 111000 nm/RIU moreover having sharp resonance peak the sensor also attains a record AS of 2050 RIU^{-1}. To the best of our knowledge the obtained WS and AS is maximum with minimum CL in the literature of biosensing. Also note that, we characterized the sensor for an analyte RI from 1.33 to 1.43, one of the reason is most of the biochemical and biomedical analytes varies within the RI range of 1.33 to 1.43 [11, 12]. Moreover, we can see from Fig. 5 (a) that the loss peak broadens for analyte RI of 1.43 that leads to low amplitude sensitivity of around 120 RIU^{-1} (Fig. 5 (b)). Therefore we characterise the sensor for an RI of upto 1.43 because further increase may lead to false detection of analytes due to such broadening of the loss peak.

The proposed sensor shows the full-width-half-maximum (FWHM) values are 130, 82, 71, 63, 55, 52, 47, 48, 59 and 138 for analyte RI of 1.33 to 1.42 respectively. With the increase of analyte RI, resonance peak becomes sharper however, after a certain RI loss spectra start broadening. Moreover, the linearity of the proposed sensor upto RI of 1.43 is $R^2 = 0.7789$ however a more linear characteristics $R^2 = 0.9662$ is obtained upto RI of 1.42 (Fig. 5 (c)). In addition, the linearity between 1.42 and 1.43 also shown in inset Fig. 5 (c) where the obtained R^2 is 0.9996.

The sensor length is an important consideration that varies in proportion to CL. Accordingly, for an analyte RI from 1.33 to 1.43 the proposed sensor shows a high sensor length of 217, 181, 145, 106, 75, 50, 31, 17, 8, 3, and 0.27 cm respectively. Note that high sensor length is suitable for practical sensing.

The sensor resolution and LOD are also two important factors in biosensing which control the extent to which the sensor can precisely detect small changes in sizes and nearby RI [7, 13]. Considering $\lambda_{\text{min}} = 0.1$ nm, according to WS the maximum resolution of the sensor goes upto 9×10^{-7} RIU. Therefore the sensor can detect a tiny change of environmental RI variation that is of the order of 10^{-7}. Moreover, based on the obtained maximum resolution the maximum LOD of the sensor is 8.12×10^{-12} RIU^2/nm that are best in the literature of biosensing.

In summary, we proposed a low loss, highly sensitive LSPR-PCF based sensor for SERS response intensification in the visible to mid-IR spectrum. We demonstrated the way how we obtained a sensor design with optimized geometrical parameters. Our study shows, the sensor can attain a record WS and AS of 111000 nm/RIU and 2050 RIU^{-1} with maximum sensor resolution and LOD of 9×10^{-7} RIU and 8.12×10^{-12} RIU^2/nm respectively. As shown in Fig. 1 (b) the proposed sensor can be made using capillary stacking and open new possibilities for highly sensitive and precise detection of bioanalytes.

Funding Information
Funding from the Australian Research Council (DP170104984) is gratefully acknowledged.

REFERENCES

1. S. A. Maier, P. G. Kik, H. A. Atwater, S. Meltzer, E. Harel, B. E. Koel, and A. A. Requicha, Nat. Mater., 2(4), 229-232 (2003).
2. Y. Kalachyova, O. Lyutakov, M. Kostejn, M. Clupek, V. Svorcik, Electronic Materials Letters, 11(2), 288-294 (2015).
3. S. Zou, N. Janel, and G. C. Schatz, J. Chem. Phys., 120(23), 10871-10875 (2004).
4. H. Wang, H. Zhang, J. Dong, S. Hu, W. Zhu, W. Qiu, H. Lu, J. Yu, H. Guan, S. Gao, Z. Li, W. Liu, M. He, J. Zhang, Z. Chen, and Y. Luo, Photon. Res., 6(6), 485-491 (2018).
5. S. Cao, Y. Shao, Y. Wang, T. Wu, L. Zhang, Y. Huang, F. Zhang, C. Liao, J. He, and Y.Wang, Opt. Express, 26(4), 3988-3994 (2018).
6. A. A. Rifat, F. haider, R. Ahmed, G. A. Mahdiraji, F. R. M. Adikan, and A. E. Miroshnichenko, Opt. Lett., 43(4), 891–894 (2018).
7. D. Paul, R. Biswas, Optics & Laser Technology , 101, 379-387(2018).
8. Md. S. Islam, J. Sultana, Ahmmed. A. Rifat, R. Ahmed, A. Dinovitser, Brian W.-H. Ng, H. Ebendorff-Heidepriem, and D. Abbott, Optics Express, 26(21), 30347-30361(2018).
9. J. Lu, Y. Li, Y. Han, Y. Liu, and J. Gao, Appl. Opt., 57(19), 5268–5272 (2018).
10. Ahmmed A. Rifat, G. A. Mahdiraji, Yong Meng Sua, Rajib Ahmed, Y. G. Shee, and F. R. Mahamd Adikan, Opt. Express, 24(3), 2485-2495(2016).
11. A. Aray, F. Chiavaioli, M. Arjmand, C. Trono, S. Tombelli, A. Giannetti, N. Cennamo, M. Soltanolkotabi, L. Zeni, and F. Baldini, J. Biophoton., 9(10), 1077–1084(2016).
12. A. K. Yetisen, H. Butt, T. Mikulchyk, R. Ahmed, Y. Montelongo, M. Humar, N. Jiang, S. Martin, I. Naydenova, and S. H. Yun, Adv. Opt. Mat., 4(10), 1589–1600(2016).
13. I. M. White and Xudong Fan, Opt. Express, 16(2), 1020–1028 (2008).
14. J. R. DeVore, J. Opt. Soc. Am., 41(6), 416–419, (1951).
15. A. Vial, A.-S. Grimault, D. Macías, D. Barchiesi, M. L. de la Chapelle, Phys. Rev. B, 8(6), 085416, (2005).
16. Berge Tatian, Appl. Opt., 23(24), 4477–4485, (1984).

1. FULL REFERENCES

REFERENCES

1. S. A. Maier, P. G. Kik, H. A. Atwater, S. Meltzer, E. Harel, B. E. Koel, and A. A. Requicha, "Local detection of electromagnetic energy transport below the diffraction limit in metal nanoparticle plasmon waveguides," *Nat. Mater.*, vol. 2, no. 4, pp. 229-232, 2003.
2. Y. Kalachyova, O. Lyutakov, M. Kostejn, M. Clupek, V. Svorcik, "Silver nanostructures: From individual dots to coupled strips for the tailoring of SERS excitation wavelength from near-UV to near-IR," *Electronic Materials Letters*, vol. 11, no. 2, pp. 288-294, 2015.
3. S. Zou, N. Janel, and G. C. Schatz, "Silver nanoparticle array structures that produce remarkably narrow plasmon lineshapes," *J. Chem. Phys.*, vol. 120, no. 23, pp. 10871-10875, 2004.
4. H. Wang, H. Zhang, J. Dong, S. Hu, W. Zhu, W. Qiu, H. Lu, J. Yu, H. Guan, S. Gao, Z. Li, W. Liu, M. He, J. Zhang, Z. Chen, and Y. Luo, "Sensitivity-enhanced surface plasmon resonance sensor utilizing a tungsten disulfide (WS2) nanosheets overlayer," *Photon. Res.*, vol. 6, no. 6, pp. 485-491, 2018.
5. S. Cao, Y. Shao, Y. Wang, T. Wu, L. Zhang, Y. Huang, F. Zhang, C. Liao, J. He, and Y.Wang, "Highly sensitive surface plasmon resonance biosensor based on a low-index polymer optical fiber," *Opt. Express*, vol. 26, no. 4, pp. 3988-3994, 2018.
6. A. A. Rifat, F. haider, R. Ahmed, G. A. Mahdiraji, F. R. M. Adikan, and A. E. Miroshnichenko, "Highly sensitive selectively coated photonic crystal fiber-based plasmonic sensor," Opt. Lett. **43**(4), 891–894, 2018.
7. D. Paul, R. Biswas, "Highly sensitive LSPR based photonic crystal fiber sensor with embodiment of nanospheres in different material domain, " Optics & Laser Technology, vol. 101, pp. 379-387, 2018.
8. Md. S. Islam, J. Sultana, Ahmmed. A. Rifat, R. Ahmed, A. Dinovitser, Brian W.-H. Ng, H. Ebendorff-Heidepriem,and D. Abbott, , "Dual-Polarized Highly Sensitive Plasmonic Sensor in the Visible to Near-IR Spectrum," *Optics Express*, vol. 26, no. 21, (2018)(In press).
9. J. Lu, Y. Li, Y. Han, Y. Liu, and J. Gao, "D-shaped photonic crystal fiber plasmonic refractive index sensor based on gold grating, " Appl. Opt. **57**(19), 5268–5272, 2018.
10. Ahmmed A. Rifat, G. A. Mahdiraji, Yong Meng Sua, Rajib Ahmed, Y. G. Shee, and F. R. Mahamd Adikan, "Highly sensitive multi-core flat fiber surface plasmon resonance refractive index sensor, " Opt. Express , vol. 24, no. 3, pp. 2485-2495, 2016.
11. A. Aray, F. Chiavaioli, M. Arjmand, C. Trono, S. Tombelli, A. Giannetti, N. Cennamo, M. Soltanolkotabi, L. Zeni, and F. Baldini, "SPR-based plastic optical fibre biosensor for the detection of C-reactive protein in serum," *J. Biophoton.*, vol. 9, no. 10, pp. 1077–1084, 2016.
12. A. K. Yetisen, H. Butt, T. Mikulchyk, R. Ahmed, Y. Montelongo, M. Humar, N. Jiang, S. Martin, I. Naydenova, and S. H. Yun, "Color-selective 2.5D holograms on large-area flexible substrates for sensing and multilevel security," *Adv. Opt. Mat.*, vol. 4, no. 10, pp. 1589–1600, 2016.
13. I. M. White and Xudong Fan, "On the performance quantification of resonant refractive index sensors," *Opt. Express*, vol. 16, no. 2, pp. 1020–1028, 2008.
14. J. R. DeVore, "Refractive Indices of Rutile and Sphalerite," *J. Opt. Soc. Am.*, vol. 41, no. 6, pp. 416–419, 1951.
15. A. Vial, A.-S. Grimault, D. Macías, D. Barchiesi, M. L. de la Chapelle, "Improved analytical fit of gold dispersion: Application to the modeling of extinction spectra with a finite-difference time-domain method," *Phys. Rev. B*, vol. 8, no. 6, 085416, 2005.
16. Berge Tatian, "Fitting refractive-index data with the Sellmeier dispersion formula," *Appl. Opt.*, vol. 23, no. 24, 4477–4485, 1984.